Acta Mechanica Sinica (2012) 28(6):1557–1571
DOI 10.1007/s10409-012-0210-8

RESEARCH PAPER

The effect of phase angle and wing spacing on tandem flapping wings

Timothy M. Broering · Yong-Sheng Lian

Received: 26 March 2012 / Revised: 29 September 2012 / Accepted: 8 October 2012

Abstract In a tandem wing configuration, the hindwing often operates in the wake of the forewing and, hence, its performance is affected by the vortices shed by the forewing. Changes in the phase angle between the flapping motions of the fore and the hind wings, as well as the spacing between them, can affect the resulting vortex/wing and vortex/vortex interactions. This study uses 2D numerical simulations to investigate how these changes affect the leading dege vortexes (LEV) generated by the hindwing and the resulting effect on the lift and thrust coefficients as well as the efficiencies. The tandem wing configuration was simulated using an incompressible Navier–Stokes solver at a chord-based Reynolds number of 5 000. A harmonic single frequency sinusoidal oscillation consisting of a combined pitch and plunge motion was used for the flapping wing kinematics at a Strouhal number of 0.3. Four different spacings ranging from 0.1 chords to 1 chord were tested at three different phase angles, 0°, 90° and 180°. It was found that changes in the spacing and phase angle affected the timing of the interaction between the vortex shed from the forewing and the hindwing. Such an interaction affects the LEV formation on the hindwing and results in changes in aerodynamic force production and efficiencies of the hindwing. It is also observed that changing the phase angle has a similar effect as changing the spacing. The results further show that at different spacings the peak force generation occurs at different phase angles, as do the peak efficiencies.

Keywords Tandem · Flapping · Airfoils · Micro air vehicle · Caculational fluid dynamics (CFD) · Overlapping grids

List of symbols

A	Planform area with unit depth
C_{L}	Lift coefficient
C_{P}	Power coefficient
C_{R}	Resultant coefficient
C_{T}	Thrust coefficient
f	Flapping frequency
h_0	Plunging amplitude
$h(t)$	Plunging displacement
L	Instantaneous lift force
M	Instantaneous pitching moment
p	Pressure
t	Time
T	Flapping period
u	Flow velocity
k	Reduced frequency
St	Strouhal number
V	Instantaneous plunge velocity
α_{ave}	Average angle of attack
α_0	Pitching amplitude
$\alpha(t)$	Pitching angle
η_{L}	Lift efficiency
η_{P}	Propulsive efficiency
ν	Kinematic viscosity
ρ	Fluid density
ϕ_α	Pitching phase lag
ϕ_h	Plunging phase lag
ψ	Phase angle
ω	Instantaneous rotational velocity

T. M. Broering · Y.-S. Lian (✉)
Department of Mechanical Engineering,
University of Louisville, Louisville, KY, 40292, USA
e-mail: yongshenglian@gmail.com

1 Introduction

Dragonflies are capable flying insects that utilize two pairs of independently actuated wings, with the hind set of wings operating in the wake of the fore set of wings. They are one of the fastest and most maneuverable flying insects, with measured flight speeds of up to 10 m/s and instantaneous accelerations up to $4g$ [1]. Tethered dragonflies have even been measured producing up to 20 times their body weight in lift forces [2]. Their impressive flight capabilities have generated interest in the study of flapping tandem wing configurations as a basis for the design of micro air vehicles (MAVs) that operate at similar Reynolds numbers.

A significant trait of the tandem wing arrangement is that the hindwing interacts with the wake of the forewing. Experiments by Schmidt have shown that placing a non-flapping hindwing in the wake of a flapping forewing almost doubles the propulsive efficiency as compared to a forewing flapping alone [3]. Similar results were obtained by Bosch through theoretical analysis and by Tuncer and Platzer using caculational fluid dynamics (CFD) analysis [4, 5].

Rather than employing a fixed set of hindwings, dragonflies flap both pairs of wings. Because both pairs of wings are independently actuated, the dragonfly can adjust the phase angle, ψ, between the flapping motions of the fore and the hind wings. By observing dragonflies in flight, Alexander [6] noted that they frequently make use of phase shifting; flapping inphase ($\psi = 0^\circ$) during takeoff or under maneuvers and flapping out of phase in cruising flight. Further observations by Ruppell [7], Azuma and Watanabe [8], and Thomas et al. [9] have noticed similar behavior, and it has been postulated that flapping inphase allows for high force production while flapping out of phase allows for increased efficiency, with the hindwing extracting energy from the wake of the forewing [6, 10].

The correlation between the phase angle and flight mode in dragonflies has led to a number of studies concerning the relationship between the phase angle and the force production of tandem flapping wing configurations, both experimentally and computationally. Most studies have focused on tandem wings in hovering motion [11–17]. Results by Wang and Russell [14] and Lan and Sun [15] both show that the maximum resultant force is produced when the wings flap inphase, while Wang and Russell also show that the highest efficiency is achieved when the wings flap with a phase angle near 180°. Usherwood and Lehmann [11] experimentally demonstrated that certain phase angles increase the efficiency of the tandem wing, but in their case, the maximum efficiency was achieved at $\psi = 90^\circ$. They concluded that this increase in efficiency was due to energy extraction of the hindwing from the wake of the forewing by removing swirl. Meanwhile, most of these studies show that the lift of both the fore and the hind wings is noticeably reduced compared with that of a single wing at most phase angles [11, 12, 15, 16].

The relationship between force production and the phase angle has also been studied for tandem wings in forward flight experimentally [18–21] and numerically [22–24]. Studies by both Akhtar et al. [22] and Warkentin and Delaurier [18] showed that for certain phase angles, the propulsive efficiency of the tandem wing arrangement was almost double that of a single wing. This mirrors the results mentioned earlier by Schmidt [3], Bosch [4] and Tuncer and Platzer [5]. Both Huang and Sun [23] and Wang and Sun [24] simulated 3D tandem wings at different phase angles and advance ratios, using a Navier–Stokes solver. Huang and Sun [23] found that at all advance ratios, the lift and thrust coefficients of the tandem wing were nearly constant and equal to that of a single wing when the hindwing led the forewing, but when the forewing led the hindwing, they found that the lift and thrust coefficients were noticeably reduced. Wang and Sun [24] however, demonstrated that the resultant force coefficient of the tandem configuration was noticeably lower than that of a single wing at most of the tested phase angles at all advance ratios. At each advance ratio, however, the resultant force coefficient nearly equaled that of a single wing at one of the tested phase angles, which increased from 0° to 90° as the advance ratio increased.

The dynamics by which the phase angle affects force production is often associated with variations in the wing vortex interactions between the fore and hind wings. Work by Saharon and Luttgess [19–21] with a robotic tandem wing configuration showed that adjustments in the phase angle caused variations in the vortex interactions between the fore and hind wings. While not measure forces, they hypothesized that the variations in the vortex interactions could influence force generation. Such variation in the vortex interactions has been linked to changes in the force production by other sources [12, 22, 25]. Variation in force generation due to vortex interactions with the hindwing would suggest that other parameters could also affect force generation similarly to the phase angle. Changes in the wing spacing and advance ratio could both potentially alter the point in the flapping cycle at which the hindwing interacts with vortices shed from the forewing and in turn affect the force generation. Wang and Sun [24] showed that the phase angle at which the resultant force peaked changed as the advance ratio was increased, while Maybury and Lehmann [12] saw that the phase angle at which peak lift production occurred changed as the fore and hind wings were moved closer together, though neither of the two studies attempted to link these changes in the force production specifically to altered vortex interactions. Broering et al. [25] linked the variation in force production of the hindwing to different vortex interactions between the fore and the hind wings that altered the leading edge vortex (LEV) generated by the hindwing at different phase angles. It was also observed by Rival et al. [26] that certain vortex interaction not only increased thrust but also allowed the hindwing to extract energy from the forewing. Finally, Lim and Tay simulated a tandem configuration in forward flight at different phase angles as

well as different spacings between the fore and hind wings. They demonstrated that at an optimum spacing and phase angle, the tandem wing has better performance than the single wing. They also described how the variations in vortex interactions between the two wings affected the force coefficients and efficiencies [27].

In this study, the spacing between the fore and hind wings is adjusted and its effect on the relationship among the phase angle, force production and efficiency is investigated using 2D numerical simulations. Three different phase angles, 0°, 90°, and 180° (hindwing leading), are simulated at four different wing spacings, $1.0c$, $0.5c$, $0.25c$, $0.1c$. All cases are simulated at a Reynolds number of 5 000. The shape of the airfoils is that of a flatplate with 5% chord thickness and rounded edges. Comparisons are made to a single wing flapping with the same kinematics and at the same Reynolds number. The Strouhal number of the flapping wing kinematics is 0.3 which falls into the range of 0.2 to 0.4 used by most natural fliers [28]. Specifically, the objective of the study is to determine how changes in the wing spacing affect the resulting vortex interaction between the fore and hind wings and how that affects the force generation and efficiency.

2 Research method

2.1 Numerical method

The flow field is described by the unsteady incompressible form of the Navier–Stokes equations written in primitive-variables

$$\boldsymbol{u}_t + (\boldsymbol{u}\cdot\nabla)\boldsymbol{u} + \nabla p = \nu\Delta\boldsymbol{u}, \tag{1}$$

$$\nabla\cdot\boldsymbol{u} = 0, \tag{2}$$

where $\boldsymbol{u}$ is the flow velocity, p is the pressure, ν is the kinematic viscosity, and Δ represents the Poisson operator. To avoid the checker-board instability problem associated with direct discretization of the pressure term, the above equations are rewritten in the following so called "velocity-pressure" formulation [29],

$$\boldsymbol{u}_t + (\boldsymbol{u}\cdot\nabla)\boldsymbol{u} + \nabla p - \nu\Delta\boldsymbol{u} = 0, \tag{3}$$

$$\Delta p - (\nabla\boldsymbol{u}\cdot u_x + \nabla V\cdot u_y + \nabla\omega\cdot u_z) - C_{\mathrm{d}}(\nu)\nabla\cdot\boldsymbol{u} = 0. \tag{4}$$

The new formulation is solved using the split-step approach which decouples the solution of the velocity variables from that of the pressure. In the velocity-pressure formulation the term $C_{\mathrm{d}}(\nu)\nabla\cdot\boldsymbol{u}$ is added to damp the divergence. Spatial discretization was carried out over composite overset computational grids using a second order accurate central difference. Time integration was performed by an Adams–Bashforth–Moulton predictor-corrector method. For the predictor step we use a semi–implicit scheme which discretizes the viscous terms using a Crank–Nicholson treatment and the convection terms using an Adam–Bashforth predictor-corrector. The predictor step is

$$\frac{\boldsymbol{u}^{\mathrm{p}}-\boldsymbol{u}^n}{\Delta t} = \frac{3}{2}\boldsymbol{f}_{\mathrm{E}}^n - \frac{1}{2}\boldsymbol{f}_{\mathrm{E}}^{n-1} + \alpha A\boldsymbol{u}^{\mathrm{p}} + (1-\alpha)A\boldsymbol{u}^n, \tag{5}$$

and the Adams–Moulton corrector step is

$$\frac{\boldsymbol{u}^{\mathrm{c}}-\boldsymbol{u}^n}{\Delta t} = \frac{1}{2}\boldsymbol{f}_{\mathrm{E}}^{\mathrm{p}} - \frac{1}{2}\boldsymbol{f}_{\mathrm{E}}^n + \alpha A\boldsymbol{u}^{\mathrm{c}} + (1-\alpha)A\boldsymbol{u}^n, \tag{6}$$

where superscripts "p" and "c" represent the predicted and corrected values, respectively, and $f_{\mathrm{E}} = -(\boldsymbol{u}\cdot\nabla)\boldsymbol{u} - \nabla p$ and $A\boldsymbol{u} = \nu\Delta\boldsymbol{u}$. α was set to 0.5, which gives a second order Crank–Nicolson method. An iterative solver, PETSc, is used to solve the discretized system of equations [30].

For the Reynolds number studied, 5 000, the flow was assumed to be laminar and no turbulence model was employed. While a Reynolds number of 5 000 is too high to be considered purely laminar, several studies show only small differences in the force histories when a laminar model is used compared to a turbulent model at Reynolds numbers below 60 000 [31–34].

2.2 Overlapping moving grid method

The wing flapping motion leads to a moving boundary problem. A moving grid approach is needed to dynamically update the computational grid to accommodate the wing motion, and thus an overlapping moving grid method is adopted [35]. This method enables the use of boundary-conforming structured grids to achieve high quality representation of the boundaries associated with the airfoil surface while still allowing the use of Cartesian grids to represent the flow field so that the efficiencies inherent to such grids can be exploited.

In the overlapping grid method, interpolation points are located in the overlapping region between different grids and are used to couple the solutions. As the body moves, the grid associated with the body moves with it, meaning that only the interpolation points between overlapping grids should be recalculated as opposed to the need to regenerate the whole mesh.

Figure 1 shows a schematic of the overlapping grid used for the tandem wing analysis. An O-type grid was generated around the airfoil using a hyperbolic grid generation technique. A high resolution wake grid was used to capture the wake structures between the airfoils. The fine wake grid and background grids are all of uniform density. The airfoils have the smallest grid spacing, with each subsequent grid having a larger grid spacing up to the coarse background grid which has the largest grid spacing. The entire domain is 20 chord lengths in the x and y directions with the tandem configuration centered in the domain. For the inlet boundary on the left a Dirichlet boundary condition ($u = U_0$) was assigned while on the right side, as well as the top and bottom, a zero gauge pressure outlet condition was used.

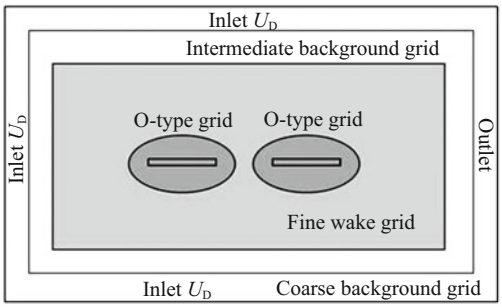

Fig. 1 Schematic of the computational grid and boundary conditions used in the study (not shown to scale)

2.3 Tandem airfoil kinematics

The flapping kinematics used in the study was a combination of sinusoidal pitching and plunging, with the pitch axis at $0.25c$ from the leading edge. It was not the intent of the study to exactly replicate dragonfly kinematics, which can vary widely depending on the flight mode and trajectory [36], but rather to study a tandem configuration undergoing simple periodic motion to reveal the pertinent wing/vortex and vortex/vortex interaction features. The flapping kinematics used were

$$\alpha(t) = \alpha_0 \cos(2\pi f t + \phi_\alpha + \phi_h) + \alpha_{\text{ave}}, \quad (7)$$

$$h(t) = h_0 \cos(2\pi f t + \phi_h), \quad (8)$$

where $\alpha(t)$ is the pitching angle, $h(t)$ is the plunging displacement, t is time, f is the flapping frequency, α_0 is the pitching amplitude, h_0 is the plunging amplitude, ϕ_α is the phase for pitch, α_{ave} is the average angle of attack (AoA), and ϕ_h is the phase for plunge. The parameters used in the kinematics for the single, fore and hind wings are shown in Table 1.

Table 1 Values used for the parameters appearing in the kinematic equations

Parameter	Single/Fore	Hind
$\alpha_0/(^\circ)$	20	20
f/Hz	0.3	0.3
$\phi_\alpha/(^\circ)$	90	90
$\alpha_{\text{ave}}/(^\circ)$	5	5
h_0/c	0.5	0.5
$\phi_h/(^\circ)$	0	0, 90, 180
St	0.3	0.3
k	0.942	0.942

The chosen frequency and plunge amplitude result in a Strouhal number of 0.3. The phase angle between pitch and plunge, ϕ_α, was chosen to be 90° (pitch leading plunge) which has been shown to be most efficient for flapping wings from a number of sources [37, 38]. The average angle of attack was so set that a moderate value of cycle averaged lift was produced. The chord-based Reynolds number was 5 000, which is in the middle range of Reynolds number for dragonflies. The flapping Reynolds number, defined as $2\pi f h_0 c/\nu$, was equal to 4 712. The kinematic parameters used for the single wing are the same as those used for the fore and hind wings.

3 Results

3.1 Grid sensitivity analysis

The numerical code used for the analysis was validated in a previous study [25]. A grid sensitivity analysis was performed to determine the grid resolution necessary to provide accurate force data as well as to resolve the flow field around the airfoils. The wall boundaries were spaced 20 chords lengths away from the airfoil, which was determined to be sufficient in a previous study [25]. The same kinematics were used for a sensitivity analysis as were used for the tandem wing cases, but only a single airfoil was used for the sensitivity analysis. In the study we systematically tested the effect of domain size and grid resolution of each individual overlapping grid, but here we only report the results from different airfoil grid resolutions. Coarse, medium and fine airfoil grid resolutions were tested respectively with 100×50, 150×75 and 200×100 grid lines in the circumferential and radial directions. A fourth type of grid was also tested, with an airfoil grid that had the same grid resolution as the medium grid (O-type grid in Fig. 1), but a smaller domain (fewer grid lines in the normal direction) and a finer wake grid resolution. As will become clear, the fourth type of grid is well suited to the tandem wing study.

Figure 2 shows the lift and thrust coefficients over a single flapping cycle for different grid types. Changing the airfoil grid resolution did not have a significant effect on the force data, with a difference less than 2% between the cycle averaged values for medium and fine grids. There was also very little difference in the force data between the results from the medium grid and the small airfoil grid, however, the wake grid density had a large effect on the flow field. Figure 3 shows that the resulting vorticity contours depended greatly on the grid type adopted. Using the medium wake grid (Fig. 3a), the vortices dissipate quickly as they move downstream; but the smaller sized airfoil grid with the fine resolution wake grid produced even better results, showing well defined vortex structures in the wake (Fig. 3c). Since the hindwing performance can be significantly affected by the shed vortices from the forewing, it is critical to capture the vortex structure. Based on the sensitivity analysis, it was decided to adopt the grid type that uses the smaller sized airfoil grid and a fine resolution wake grid for the tandem wing analysis.

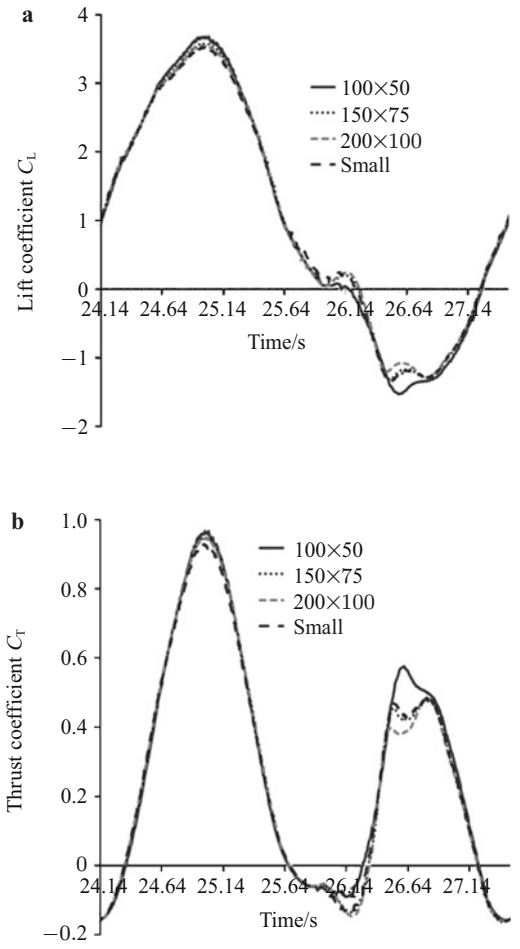

Fig. 2 Lift and thrust data for different grid types used in the sensitivity analysis. **a** Lift; **b** Thrust

Fig. 3 Vorticity contours for the different grid types used in the sensitivity analysis. A fine wake grid can better resolve the wake flow structure. **a** Medium resolution wake grid; **b** Fine resolution wake grid and a smaller sized airfoil grid

3.2 Aerodynamic force results

The lift, thrust and resultant coefficients were calculated for each wing individually as

$$C_{\mathrm{L}} = \frac{L}{0.5\rho A U^2}, \tag{9}$$

$$C_{\mathrm{T}} = \frac{T}{0.5\rho A U^2}, \tag{10}$$

$$C_{\mathrm{R}} = \frac{\sqrt{L^2 + T^2}}{0.5\rho A U^2}, \tag{11}$$

where C_{L}, C_{T}, and C_{R} are the lift, thrust and resultant force coefficients, ρ is the fluid density, A is the planform area with unit depth, U is the freestream velocity, and L and T are the lift and thrust forces. Figure 4 shows the transient lift and thrust coefficients only for the hindwing over a single flapping cycle at different wing spacings for the three tested phase angles, 0°, 90° and 180° (hindwing leading). The same results for the single wing are also shown to serve as a baseline. In the plots a cycle time, t/T, of 0% is the start of the downstroke and 50% is the start of the upstroke.

The results in Fig. 4 illustrate the significant effect that changing the phase angle or wing spacing can have on the lift and thrust generation of the hindwing. The effect of the phase angle is considered first. At 0° phase angle, the lift and thrust amplitudes of the hindwing at each spacing are much higher than that in the single wing case. When the phase angle is 90°, the hindwing has higher force amplitudes than the single wing at the small spacings but not at the large spacing of 1.0c. Finally, at 180° phase lag, the hindwing has higher force amplitudes than the single wing through the upstroke but lower force amplitudes during the downstroke for small spacings. At the largest spacing, however, the hindwing has significantly lower force amplitudes than the single wing.

Next, the impact of the wing spacing is considered. In general, increasing the wing spacing causes a phase lag in both lift and thrust generation. This trend is shown clearly in the case where the fore and hind wings flap with a 90° phase lag. Both the lift and thrust show a clear phase lag in the timing of the lift and thrust generation as the spacing is increased from 0.1c to 1.0c. There is also a trend of increase in lift and thrust amplitudes as the spacing is decreased. The 180° phase case shows nearly the same trend as the 90° phase case. There is a phase lag in both the lift and thrust as the spacing is increased from 0.1c to 0.5c, just as at 90°, but increasing the spacing to 1.0c does not show the same trend in the phase lag. The 180° case also exhibits increases in the peak lift and thrust as the spacing is decreased, similar to the 90° case. The trends observed in the 90° and 180° cases are not as evident for the 0° case. While the 0° case exhibits phase lag in the timing of the force generation as the spacing is decreased, it is inconsistent. Also, the peak lift and thrust magnitudes do not show the same increasing trend as observed in the 90° and 180° cases when the spacing is decreased.

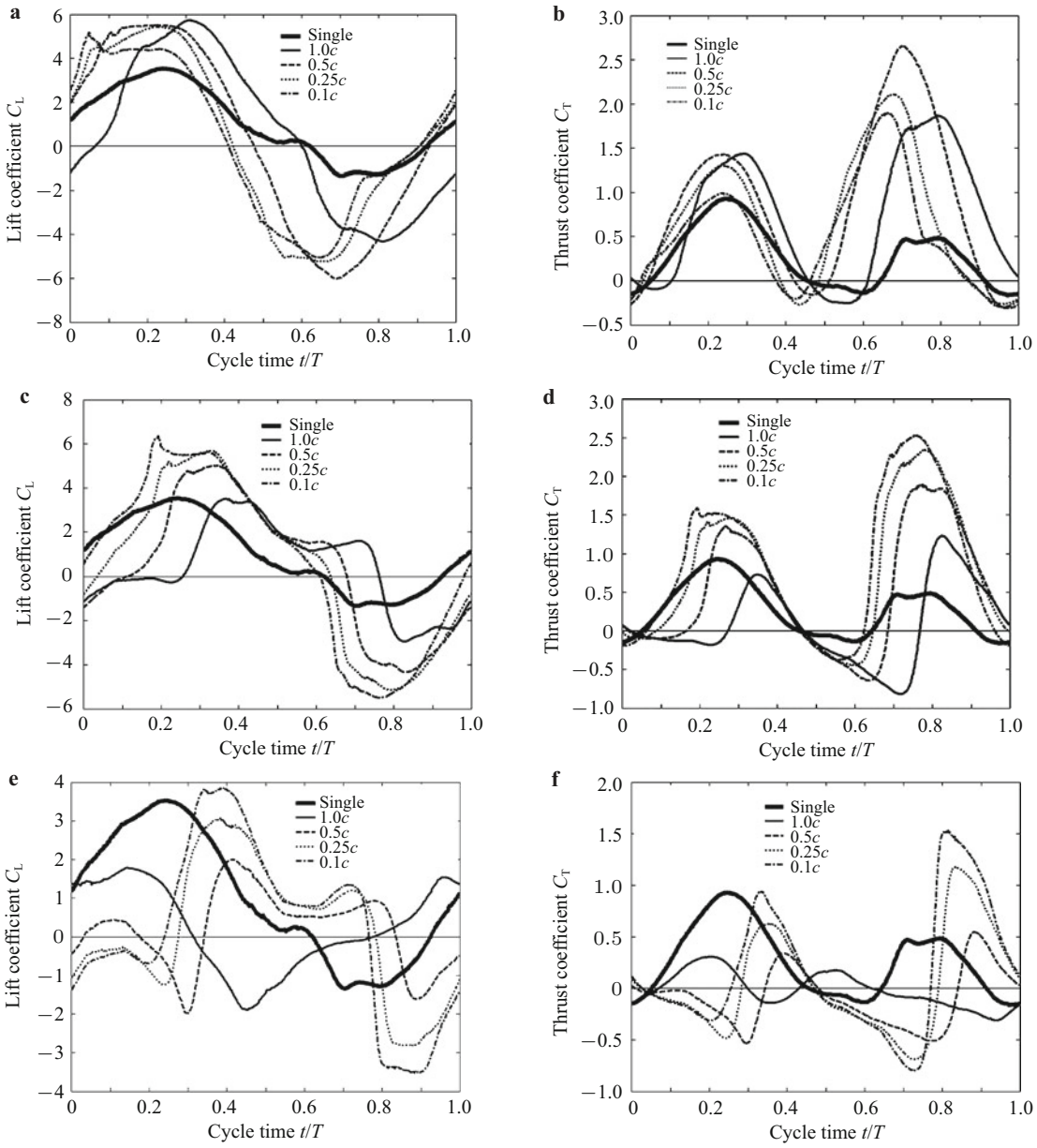

Fig. 4 Transient lift and thrust coefficients for the hindwing over a single flapping cycle compared to that for a single wing. Each graph shows the lift or thrust at a single phase angle for the four tested spacings. **a** 0° phase lift; **b** 0° phase thrust; **c** 90° phase lift; **d** 90° phase thrust; **e** 180° phase lift; **f** 180° phase thrust

3.3 Flow visualization results

The behavior observed in the force data can be explained by analyzing the vorticity contours for each case. Specifically, examining how changes in the phase angle and wing spacing changes the timing of vortex interactions during the flapping cycle of the hindwing. Figures 5–7 show the vorticity contours at different spacings for the 90°, 180° and 0° cases, respectively. For the sake of brevity, the vorticity contours are only shown for one half of the cycle (upstroke for the 90° and 180° cases and downstroke for the 0° case) as the upstroke and downstroke exhibit nearly symmetric results.

Figure 5 illustrates how changes in the wing spacing affect the timing of the vortex/wing and vortex/vortex interactions and how the interactions influence LEV formation during the upstroke of the hindwing when the wings flap with 90° phase lag. During the upstroke, the hindwing passes through a vortex shed from the trailing edge of the forewing. At closer spacings this interaction occurs in the first half of the upstroke (68% cycle time). As the spacing is increased, this vortex interaction is delayed, due to the increased time necessary for the vortex to convect to the hindwing, and occurs later in the upstroke. This delay in the vortex interaction is clearly observed as a phase lag in the transient lift and thrust data shown in Figs. 4c and 4d.

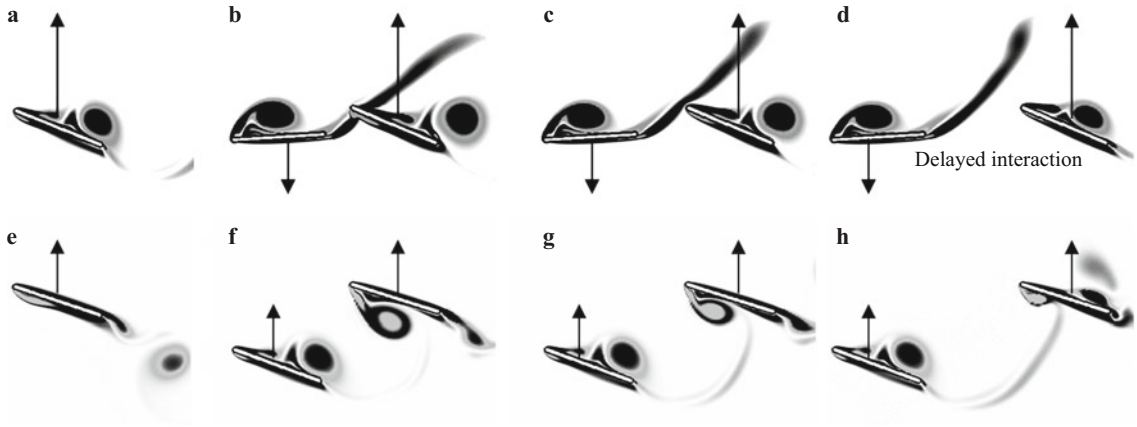

Fig. 5 The vorticity contours around the single wing and the 90° phase angle tandem configuration at different spacings. The large spacing delays and weakens the vortex/wing interaction. The first row shows the single and hind wings during the upstroke at 68% cycle time while the second row shows the single and hind wings at 89% cycle time. Arrows indicate the stroke direction. **a** Single, $t/T = 68\%$; **b** $0.25c$, $t/T = 68\%$; **c** $0.5c$, $t/T = 68\%$; **d** $1.0c$, $t/T = 68\%$; **e** Single, $t/T = 89\%$; **f** $0.25c$, $t/T = 89\%$; **g** $0.5c$, $t/T = 89\%$; **h** $1.0c$, $t/T = 89\%$

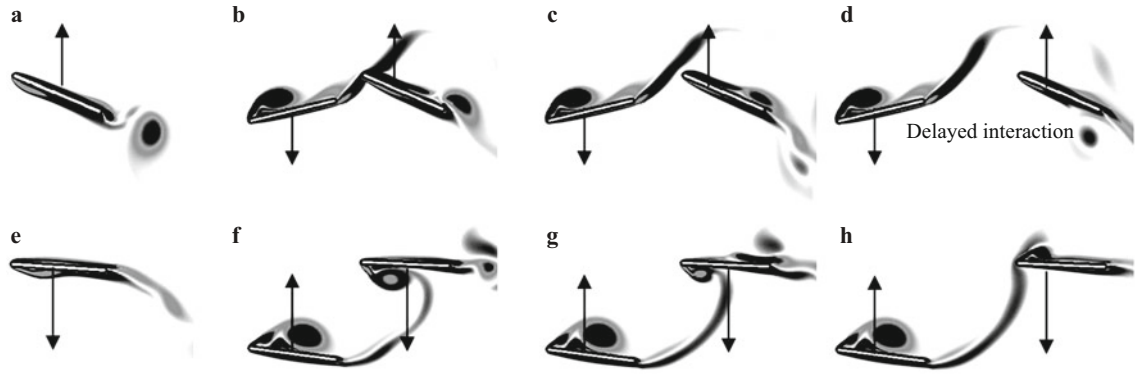

Fig. 6 The vorticity contours around the single wing and the 180° phase angle tandem configuration at different spacings. The vortex/wing interaction is delayed compared to the 90° phase angle tandem configuration case. The first row shows the single and hind wings during the upstroke at 81% cycle time while the second row shows the single and hind wings at 2% cycle time. Arrows indicate the stroke direction. **a** Single, $t/T = 81\%$; **b** $0.25c$, $t/T = 81\%$; **c** $0.50c$, $t/T = 81\%$; **d** $1.0c$, $t/T = 81\%$; **e** Single, $t/T = 2\%$; **f** $0.25c$, $t/T = 2\%$; **g** $0.5c$, $t/T = 2\%$; **h** $1.0c$, $t/T = 2\%$

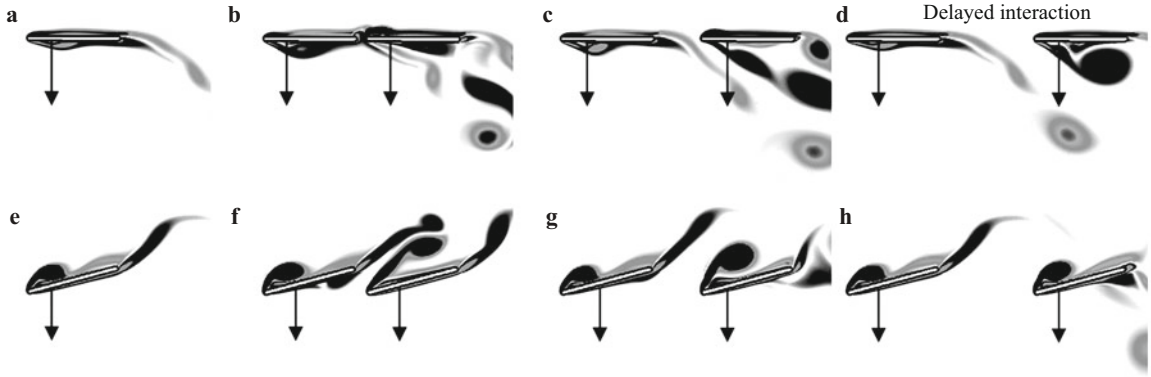

Fig. 7 The vorticity contours around the single wing and the 0° tandem configuration at different spacings. The first row shows the single and hind wings during the downstroke at 4% cycle time while the second row shows the single and hind wings at 25% cycle time. Arrows indicate the stroke direction. **a** Single, $t/T = 4\%$; **b** $0.1c$, $t/T = 4\%$; **c** $0.5c$, $t/T = 4\%$; **d** $1.0c$, $t/T = 4\%$; **e** Single, $t/T = 25\%$; **f** $0.1c$, $t/T = 25\%$; **g** $0.5c$, $t/T = 25\%$; **h** $1.0c$, $t/T = 25\%$

The timing of the interaction between the hindwing and vortex shed from the forewing has a noticeable effect on the LEV formation around the hindwing. The bottom row of Fig. 5 shows the vorticity contours when the hindwing is at 89% cycle, just before stroke reversal, after the vortex interaction has occurred. The rotation of the shed vortex is the same as the rotation of the LEV that forms on the bottom of the hindwing (counterclockwise, CCW), which reinforces the LEV generation. At closer spacings, the vortex interaction is stronger because the vortex shed from the forewing has less time to dissipate before interacting with the hindwing. This results in larger LEV generation by the hindwing, which corresponds to the increased peak in the transient lift and thrust data as the spacing is decreased. The increased peak in the transient force data can be observed in Figs. 4c and 4d. In the downstroke, the same interaction and phase lag is observed, except that the vortex shed from the forewing and the LEV generated by the hindwing are both clockwise (CW).

Similar to Fig. 5, Fig. 6 shows the vorticity contours at different spacings for the 180° phase case during the upstroke. In this case, the hindwing passes through the vortex shed by the forewing, as in the 90° case, but the vortex interaction occurs significantly later in the upstroke due to the larger phase angle. At the closest spacings, the hindwing starts to interact with the shed vortex in the second half of the upstroke, at 81% of cycle compared to 68% of cycle for the 90° case. As the spacing is increased this interaction is delayed, which corresponds to the phase lag in the force data shown in Figs. 4e and 4f. This behavior is similar to that observed in the 90° case. At 180° phase lag, however, when the wing spacing is increased to $1.0c$, the vortex interaction is delayed until after stroke reversal, which allows the start of LEV formation on top of the hindwing. The delay is reflected in the force data shown in Figs. 4e and 4f, in which the $1.0c$ spacing shows dramatically different pattern from that for other spacings.

The timing of the vortex interaction has large implications on the LEV generation of the hindwing. These implications can be observed in Figs. 6e–6h by comparing the LEVs on the hindwings. At the closest spacings, the hindwing passes through the shed vortex before stroke reversal, which serves to reinforce the LEV formation at the bottom of the hindwing (both vortices have the same rotation, CCW). As the spacing is increased, the vortex interaction becomes weaker as the vortex shed from the forewing has more time to dissipate before interacting with the hindwing, resulting in weaker LEV generation. This corresponds to lower peak lift and thrust observed in the force data as the spacing is increased, as observed in Figs. 4e and 4f. At the spacing of $1.0c$, the interaction is delayed until stroke reversal, where the hindwing starts to form a CW LEV on top. The interaction with the CCW shed vortex dampens out the CW LEV and quickens its shedding, which results in extremely low lift and thrust production observed for this case in Figs. 4e and 4f. As with the 90° case, the results for downstroke are symmetrical to that for upstroke except that the rotation of the vortices are reversed.

Figure 7 shows the vorticity contours at the tested spacings for the 0° phase case during the downstroke. The results are shown for the downstroke rather than the upstroke because the vortex interaction is easier to observe. Similar to the 90° and 180° cases, the hindwing passes through the vortex shed from the trailing edge of the forewing and the interaction is delayed as the spacing is increased. Because the fore and hind wings flap with 0° phase lag, at the smaller spacings, the two wings remain in close proximity to each other throughout the entire cycle. At the $1.0c$ and $0.5c$, the interaction between the CW shed vortex and the hindwing reinforces the formation of the CW LEV on the hindwing, which results in increased peak lift and thrust. At the closest spacings, however, a jet forms between the two plates, which quickens the LEV shedding and results in a smaller and elongated LEV at the closest spacings. This behavior is most obvious when the spacing is decreased to $0.1c$ (which is shown in Fig. 7, rather than $0.25c$). Figure 8 shows the vertical velocity profile of this jet (between the trailing edge of the forewing and the leading edge of the hindwing) for the $0.1c$ and $1.0c$ cases at 12% cycle time (the first half of the downstroke). It is clear that at the closer spacing the vertical velocity component of the jet is much stronger. The weakened LEV production at the closest spacings explains why the peak lift and thrust does not continue to increase when the spacing is decreased as in the 90° and 180° cases.

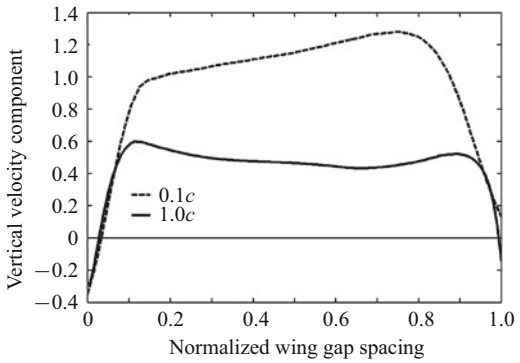

Fig. 8 The profile of the vertical velocity component taken between the trailing edge of the forewing and the leading edge of the hindwing. The results shown are for a wing spacing of $0.1c$ and $1.0c$ with the x-axis normalized by the wing spacing

3.4 Effect of vortex interaction on C_P

The effect of the vortex interaction on the pressure distribution around the airfoil is shown in Fig. 9. The y-axis is reversed so that the top of the curve corresponds to the top of the airfoil (negative pressure) and vice versa. Figure 9 compares the pressure distribution around the airfoil of both the single wing a and the hindwing at a phase angle of 0° and **a** wing spacing of $0.5c$ **b** immediately before and immediately

after the vortex interaction during the downstroke, which is the vortex interaction shown in Fig. 7. The hindwing shows a large increase in suction at the top of the leading edge that corresponds to its passing of the vortex shed by the forewing. There is no observable increase in suction for the single wing at the same point in the cycle.

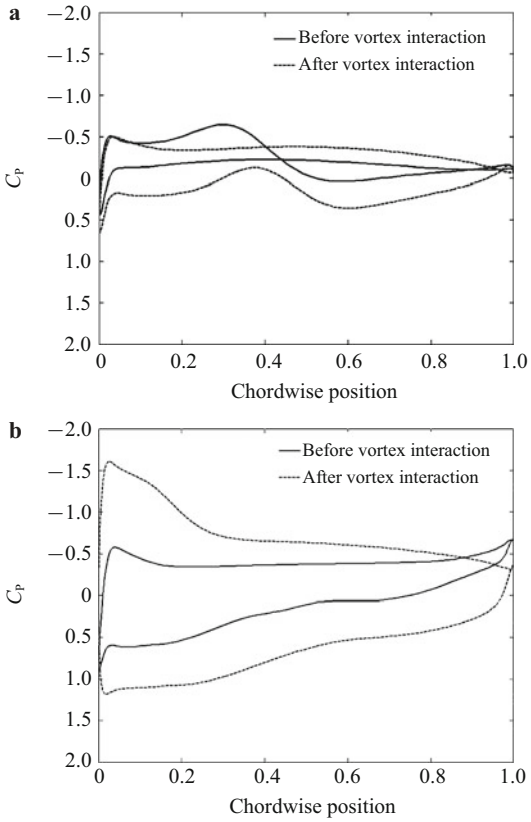

Fig. 9 There is a large increase in suction on the top of the leading edge of the hindwing that is associated with its passing through the vortex shed by the forewing. There is no observable increase for the single wing

3.5 Effect of phase angle vs. spacing

Figure 10 compares the transient lift and thrust history for the 0° phase angle case at 1.0c with that for the 90° case at 1.0c and 0.25c. Despite the difference in phase angle, the 0° case at 1.0c and the 90° case at 0.25c exhibit remarkably similar force histories. These two cases show nearly the same trend in lift and thrust generation (hence vortex and wing interactions) while the only difference between them is in peak lift and thrust production. This reveals that, in terms of force generation, decreasing the wing spacing has an effect opposite to that of increasing the phase angle. In this case, decreasing the baseline spacing from 1.0c to 0.25c while also increasing the baseline phase angle from 0° to 90° generates similar results as compared with the baseline. However, when the phase angle is increased from 0° to 90° while keeping the spacing constant at 1.0c, there is a significant change in the transient lift and thrust coefficient compared to the other two cases.

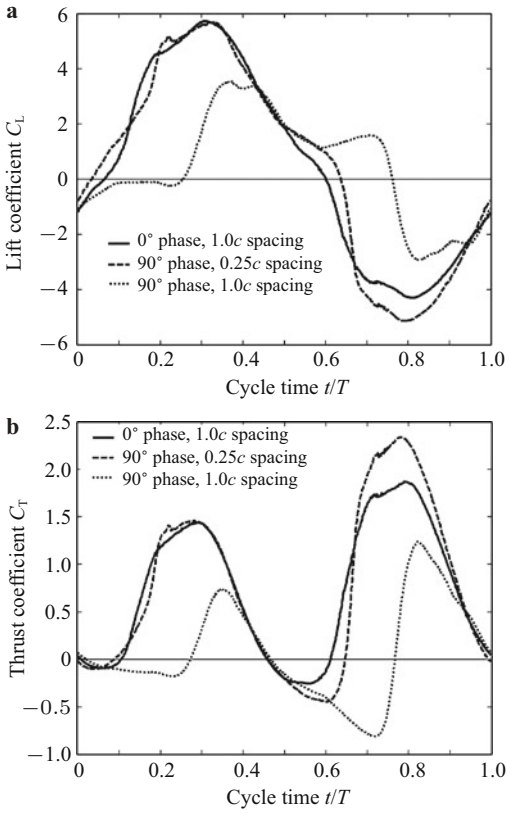

Fig. 10 Comparison of the lift and thrust over a single flapping cycle for the 0° hindwing at 1.0c with that for the 90° hindwing at 1.0c and 0.25c. **a** Lift; **b** Thrust

Figure 11 is similar to Fig. 10, except it compares the force history for the 90° phase angle case at 1.0c with that for the 180° case at 1.0c and 0.25c. Again, the resulting force histories are very similar when the phase angle is increased by 90° while simultaneously decreasing the spacing from 1.0c to 0.25c. The two cases (90° at 1.0c and 180° at 0.25c) show similar timing in force generation, but different magnitudes of peak lift and thrust. Like Fig. 10, increasing the phase angle from 0° (1.0c) to 90° (1.0c) causes a shift in force histories. However, decreasing the spacing from 1.0c (90°) to 0.25c (90°) will offset the shift. This shows that increasing the phase angle has an effect opposite to that of decreasing the spacing.

Examining the vorticity contours reveals the reason why the force histories are nearly the same between certain different cases. Figure 12 compares the vorticity contours between the 0° and 90° cases at different spacings during the upstroke. For these specific cases, the hindwing passes through the vortex shed from the forewing at nearly the same time during the upstroke, resulting in similar LEV generation on the

hindwing. Specifically, the timing of LEV generation and shedding is approximately the same between the two cases despite the difference in spacing and phase angle. This corresponds to the similar force histories observed in Fig. 11. There are slight differences in the size of the LEV, which results in difference in the peak lift and thrust observed between the two cases.

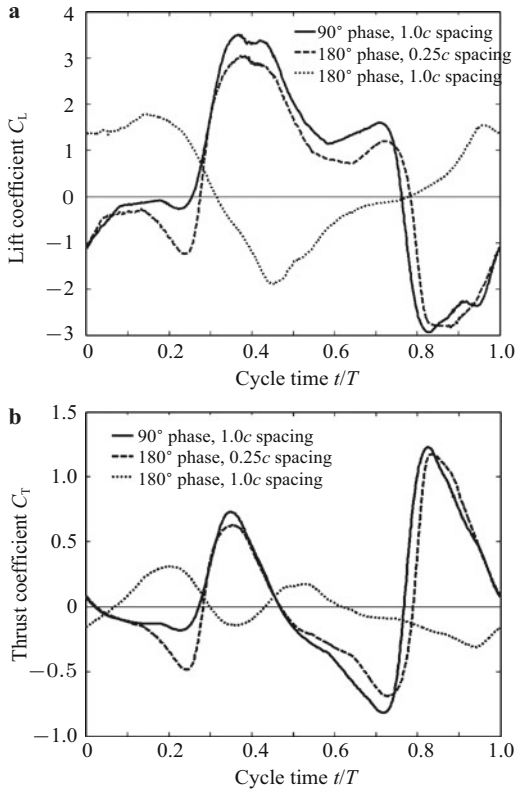

Fig. 11 Comparison of the lift and thrust over a single flapping cycle for the 90° hindwing at 1.0c with that for the 180° hindwing at 1.0c and 0.25c. **a** Lift; **b** Thrust

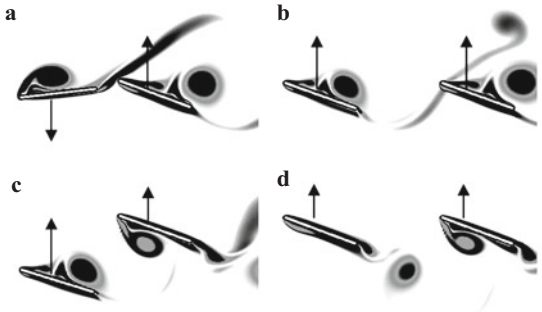

Fig. 12 Comparison of the vorticity contours for the 0° hindwing at 1.0c with that for the 90° hindwing at 0.25c and 0.1c. Despite the parameter difference, the vortex structures on the hind wing are very similar. The contours were taken during the upstroke at 65% and 86% of the cycle time. Arrows indicate the stroke direction. **a** 90°, 0.25c, t/T = 65%; **b** 0°, 1.0c, t/T = 65%; **c** 90°, 0.25c, t/T = 86%; **d** 0°, 1.0c, t/T = 86%

Figure 13 shows similar results to Fig. 12 for the 180° and 90° cases. For these two cases, although the phase angle and spacing are not the same, the timing of the vortex interaction between the fore and hind wings during the upstroke of the hindwing is nearly identical. This results in comparable LEV formation on the hindwing and the resulting similarities in the transient lift and thrust data between the 90° and 180° cases, as shown in Fig. 11. As with the 0° and 90° cases, there are slight differences in the size of the LEV generated, which result in differences observed in the peak lift and thrust.

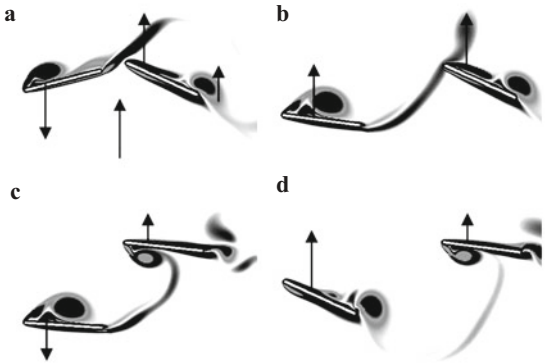

Fig. 13 Comparison of the vorticity contours for the 0° hindwing at 1.0c with that for the 90° hindwing at 0.25c and 0.1c. Again, vortex structures on the hindwing are very similar, despite the parameter difference. The contours were taken during the upstroke at 77% and 98% of the cycle time. Arrows indicate the stroke direction. **a** 180°, 0.25c, t/T = 77%; **b** 90°, 1.0c, t/T = 77%; **c** 180°, 0.25c, t/T = 98%; **d** 90°, 1.0c, t/T = 98%

3.6 Cycle averaged force results

The cycle averaged lift, thrust and resultant coefficients were calculated over a single flapping cycle for the hindwing at each phase angle, and plotted versus the spacing. These, along with the time averaged power coefficient and lift and propulsive efficiencies, are shown in Fig. 14. The cycle averged power coefficient, which is a nondimensional measurement of the power required to actuate the wing during a single flapping cycle, was calculated using

$$C_P = \frac{1}{0.5\rho A U^3} \int_0^T [-(LV) - (M\omega)]\mathrm{d}t, \tag{12}$$

where C_P is the power coefficient, ρ is the fluid density, A is the planform area with unit depth, U is the flow velocity, T is the flapping period, L is the instantaneous lift force, V is the instantaneous wing vertical velocity, M is the instantaneous pitching moment, and ω is the instantaneous rotational velocity. In Eq. (12) the power coefficient C_P is defined such that a positive C_P represents power output by the system and negative C_P is power put back into the system. As discussed by Broering et al. [25], it is impractical for the wing to regenerate power during the flapping cycle, the calculation of C_P was modified such that when the integrand

was negative it was changed to zero for the integration. So when the force opposes the motion, positive actuation power is required, and when the force is coincident with the motion, zero actuation power is required (rather than negative actuation power). Further references to C_P refer to this modified C_P. In the cases studied, the power contributed by the moment term was negligible compared to the lift term. The lift and propulsive efficiencies, were calculated using

$$\eta_P = \frac{C_T}{C_P}, \tag{13}$$

$$\eta_L = \frac{C_L}{C_P}, \tag{14}$$

where η_P is the propulsive efficiency, C_T is the thrust coefficient, η_L is the lift efficiency, and C_L is the lift coefficient.

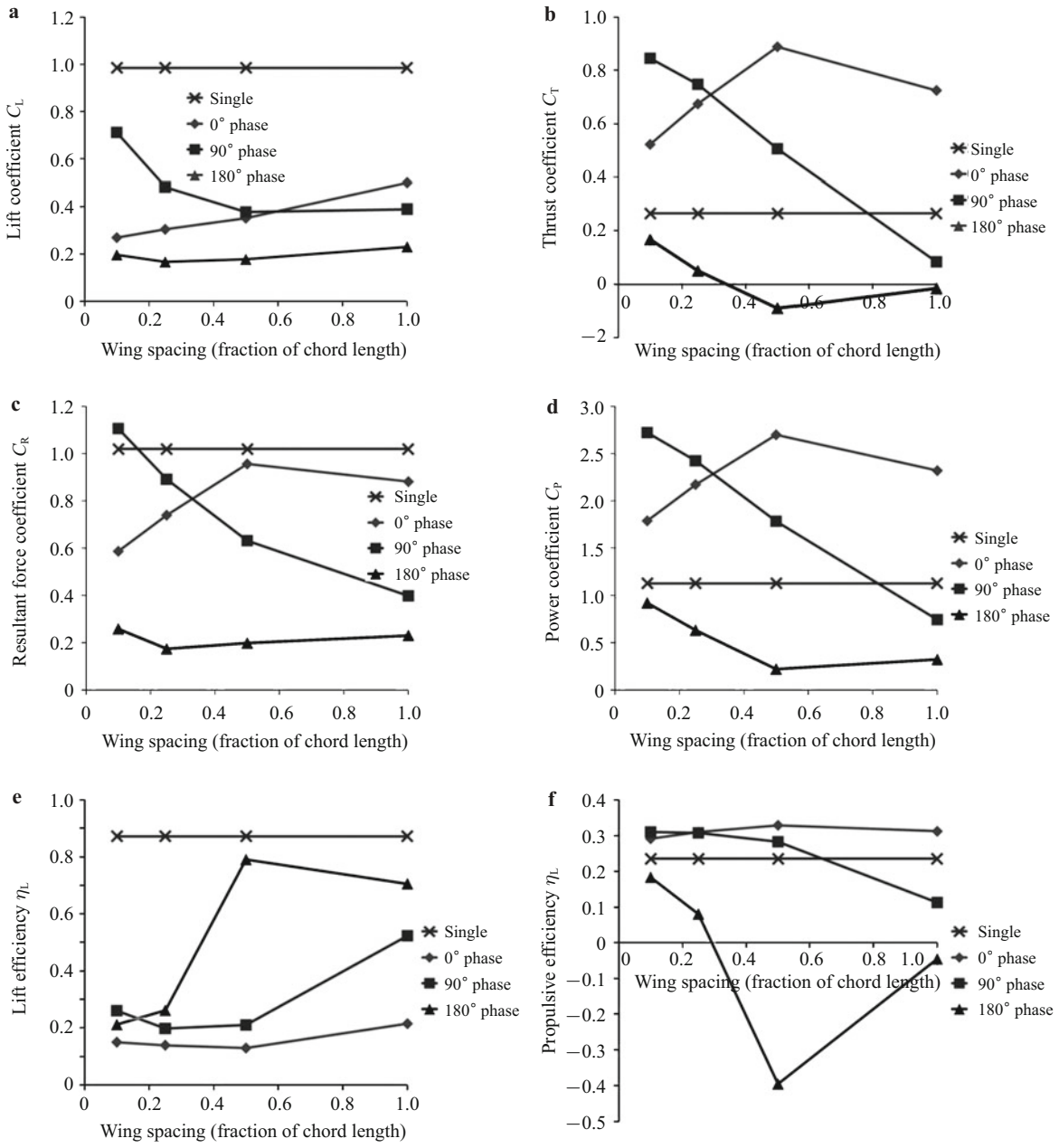

Fig. 14 Cycle averaged lift, thrust, resultant and power coefficients as well as the lift and propulsive efficiencies for the hindwing. The results are graphed vs. the spacing for the three phase angles (0°, 90°, 180°) and compared to that for the single wing. **a** Lift; **b** Thrust; **c** Resultant; **d** Power; **e** Lift efficiency; **f** Propulsive efficiency

Figure 14 demonstrates how the phase angle and spacing affect the cycle averaged force production and power consumption, as well as the efficiencies. The results for a single wing are also included to provide a baseline comparison. As shown in Fig. 14a, the hindwing has a lower lift coefficient than a single wing at all tested cases. For the 0° and 180° phase angles, the lift coefficient decreases as the spacing is decreased, but for the 90° phase angle case, the lift coefficient increases as the spacing decreases.

The hindwing in the 0° and 90° cases consistently have a significantly higher thrust coefficient (Fig. 14b) than a single wing, while the 180° hindwing has a much lower thrust coefficient than a single wing, and actually produces net drag at the farthest two spacings (0.5c and 1.0c). The 90° cases shows the most significant change in the thrust coefficient as the spacing is changed, rising nearly linearly from 0.07 at 1.0c to 0.82 at 0.1c. The 0° case shows a peak in the thrust coefficient at 0.5c and then a noticeable decrease as the spacing is further increased, while the 180° case shows a minimum thrust coefficient at 0.5c and then a significant rise in the thrust coefficient as the spacing is decreased. The resultant force coefficient (Fig. 14c) and power coefficient (Fig. 14d) at each phase angle shows a similar trend to that observed for the thrust coefficient, except that the resultant coefficient in all cases is lower than the resultant coefficient for a single wing (due to the low lift production of the hindwing in all cases), except for the resultant coefficient for the 90° hindwing at 0.1c.

In terms of efficiency, the 180° case has the highest lift efficiency at each spacing (but still less than a single wing) while the 0° case has the lowest, except at a spacing of 0.1c where the 90° case has the highest lift efficiency. The 0° and 90° cases exhibit the highest propulsive efficiencies (higher than that for a single wing) while the 180° case has the lowest (less than that for a single wing). The propulsive efficiency of the 0° case is nearly constant at all spacings while the 90° case shows a significant increase in efficiency with decreasing spacing. The 180° hindwing has a negative propulsive efficiency at the largest two spacings (net drag production), with a minimum at 0.5c, but its efficiency increases to just slightly less than that of the single wing at 0.1c.

It is interesting to note how changes in the spacing affect the relationship between phase angle and force production. At the largest spacing, 1.0c, the hindwing at 0° phase lag produces the largest lift and thrust coefficients, while the hindwing at 180° phase lag produces the smallest with the 90° hindwing falling in between the two. As the spacing is decreased, the lift and thrust coefficients rise for the 90° hindwing and fall for the 0° hindwing. At a spacing of 0.1c, the 180° hindwing still produces the smallest lift and thrust coefficients, but the 90° hindwing has the largest lift and thrust coefficients, while the 0° hindwing falls between the two. This certainly shows that the relationship between the phase angle and the force production is not consistent, but altered as the wing spacing alters.

Time averaged values of the force and power coefficients were also averaged between the fore and hind wings in order to determine the results for the tandem configuration as an integrated system. These results were also plotted for each phase angle versus the spacing in Fig. 15 to show the effect of phase angle and spacing on the performance of the entire system. For this comparison, the lift thrust and resultant coefficients were calculated using

$$C_{\mathrm{L}} = \frac{L_{\mathrm{F}} + L_{\mathrm{H}}}{0.5\rho(A_{\mathrm{F}} + A_{\mathrm{H}})U^2}, \tag{15}$$

$$C_{\mathrm{T}} = \frac{T_{\mathrm{F}} + T_{\mathrm{H}}}{0.5\rho(A_{\mathrm{F}} + A_{\mathrm{H}})U^2}, \tag{16}$$

$$C_{\mathrm{R}} = \frac{\sqrt{(L_{\mathrm{F}} + L_{\mathrm{H}})^2 + (T_{\mathrm{F}} + T_{\mathrm{H}})^2}}{0.5\rho(A_{\mathrm{F}} + A_{\mathrm{H}})U^2}, \tag{17}$$

where L, T, and A are the lift, thrust, and planform area, and the subscripts "F" and "H" denote the fore and hind wings, respectively. Since the combined force production of the tandem configuration is normalized by the planform area of both wings, the lift, thrust and resultant coefficients can be compared to the same results for a single wing.

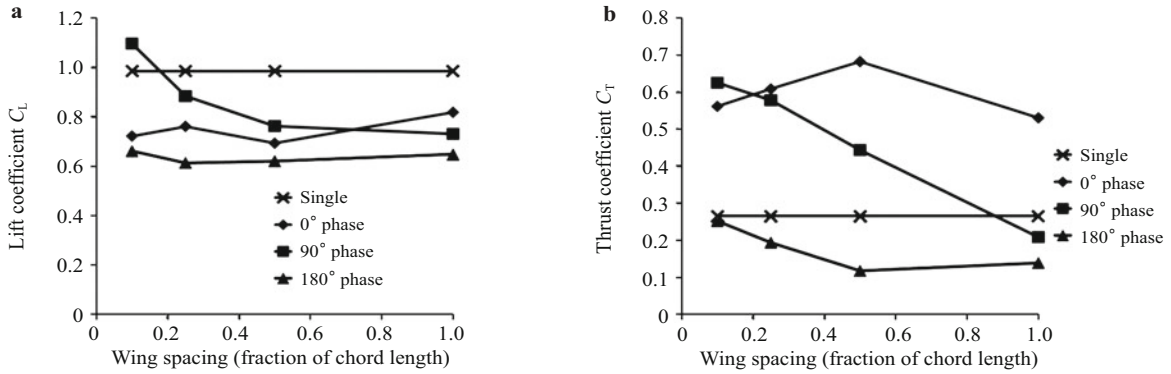

Fig. 15 Cycle averaged lift, thrust, resultant and power coefficients as well as the lift and propulsive efficiency averaged between the fore and hind wings. The results are graphed vs. the spacing for the three phase angles and compared to that of the single wing. **a** Lift; **b** Thrust; **c** Resultant; **d** Power; **e** Lift efficiency; **f** Propulsive efficiency

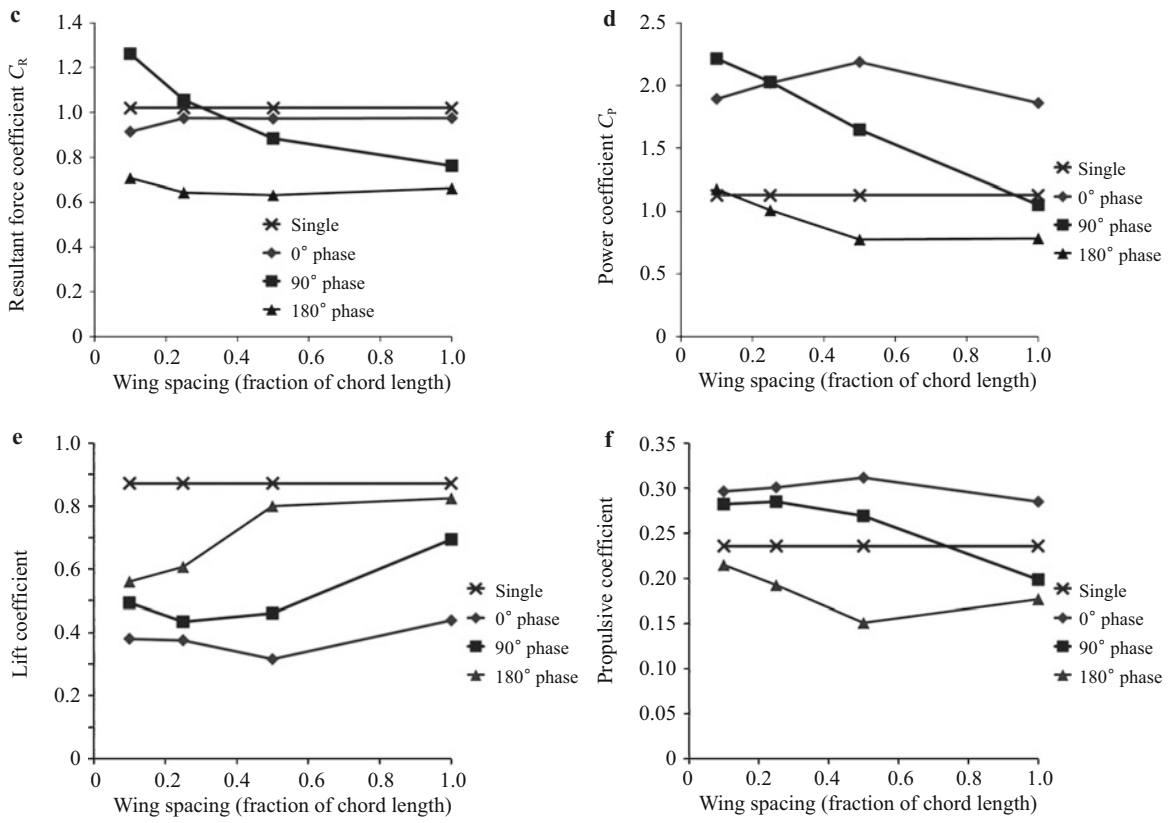

Fig. 15 Cycle averaged lift, thrust, resultant and power coefficients as well as the lift and propulsive efficiency averaged between the fore and hind wings. The results are graphed vs. the spacing for the three phase angles and compared to that of the single wing. **a** Lift; **b** Thrust; **c** Resultant; **d** Power; **e** Lift efficiency; **f** Propulsive efficiency (continued)

The averaged results of the fore and hind wings show the same trends observed for the hindwing in Fig. 14. At a spacing of 1.0c, the 0° case produces the largest lift and thrust coefficients while the 180° case produces the smallest and the 90° falls between the two. As the spacing is decreased, the lift and thrust coefficients increase significantly for the 90° case until at a spacing of 0.1c, the 90° produces the most lift and thrust and the 0° case falls in the middle. In terms of efficiency the 180° has the highest lift efficiency at all spacings (still below the lift efficiency of a single wing), while the 0° case has the lowest. The 0° case has the highest propulsive efficiency at all spacings, while the 180° case has the lowest. The 0° case at all four spacings, and the 90° at the smallest three spacings have a higher propulsive efficiency than the single wing while at all four spacings, the 180° case has a lower propulsive efficiency than the single wing.

4 Conclusion

A numerical investigation had been conducted to clarify the effects of phase lag and spacing on the vortex/wing and vortex/vortex interactions, as well as the force generation and efficiencies of a tandem wing configuration with emphasis laid on the hindwing. The results from this study suggest that the force production and efficiency of the hindwing are heavily influenced by its interaction with the wake of the forewing, and that the nature of this interaction can be controlled by adjusting both the phase angle and the spacing between the fore and hind wings. For the kinematics and flow conditions used in this paper, both the phase angle and spacing affect the specific timing at which the hindwing passes through the vortex shed from the forewing.

The interaction between the shed vortex and the hindwing also influences the LEV generation of the hindwing. Changes in the phase angle or spacing affect the timing of this interaction which, in turn, affects the timing of the generation and shedding of the LEV on the hindwing. The interaction between the shed vortex and the LEV can be described as constructive or destructive. Nearly every case studied in this paper exhibits constructive vortex interaction, where the directions of rotation of the shed vortex and the LEV are the same. This interaction reinforces the LEV and results in larger and stronger LEV formation compared with the case of single wing with no interaction. Only one case studied here exhibits destructive vortex interaction and that is the 180° case with 1.0c spacing. In this case, the directions of rotation of the shed vortex and LEV were opposite to each other. This dampens the LEV formation and quickens the shedding, resulting in the formation of a smaller LEV compared with the case of single wing without interaction. Un-

like previous studies, which typically show that peak resultant forces are generated at 0° phase angle and peak power efficiency occurs out of phase, our study shows that at different spacings the peak force generation and peak efficiencies occur at different phase angles.

The timing of the LEV generation and shedding corresponds to the phase lag observed in the lift and thrust data associated with changes in the spacing and phase angle while the size of the LEV generated corresponds to the peak lift and thrust production. This suggests that changes in the phase angle and spacing can be used to control the force production and efficiency of the hindwing by controlling its LEV formation. Both the phase angle and spacing were observed to have similar effects on the force production, which corresponded to similarities in the LEV formation and shedding. Specifically, for the cases studied, an increase in the phase angle of 90° was observed to have an effect similar to an decrease in the spacing of $0.75c$. This specific correspondence is almost assuredly a function of the flight speed and flapping kinematics used in the study.

References

1 May, M. L.: Dragonfly flight: Power requirements at high speed and acceleration. The Journal of Experimental Biology **158**, 325–342 (1991)

2 Reavis, M. A., Luttges, M. W.: Aerodynamic forces produced by a dragonfly. AIAA Journal **88-0330**, 1–13 (1988)

3 Schmidt, W.: Der Wellpropeller, ein Neuer Antrieb fuer Wasser-, Land-, und Luftfahrzeuge. Zeitschrift fur Flugwissenschaften **13**, 427–479 (1965)

4 Bosch, H.: Interfering airfoils in two-dimensional unsteady incompressible flow. AGARD-CP-277 (1977)

5 Tuncer, I. H., Platzer, M. F.: Thrust generation due to airfoil flapping. AIAA Journal **34**, 324–331 (1996)

6 Alexander, D. E.: Unusual phase relationships between forewings and hindwings in flying dragonflies. Journal of Experimental Biology **109**, 379–383 (1984)

7 Ruppell, G.: Kinematic analysis of symmetrical flight maneuvers of Odonata. The Journal of Experimental Biology **144**, 13–42 (1989)

8 Azuma, A., Watanabe, T.: Flight performance of a dragonfly. The Journal of Experimental Biology **137**, 221–252 (1988)

9 Thomas, A. L. R., Taylor, G. K., Srygley, R. B., et al.: Dragonfly flight: free-flight and tethered flow visualizations reveal a diverse array of unsteady flight-generating mechanisms, controlled primarily via angle of attack. The Journal of Experimental Biology **207**, 4299–4323 (2004)

10 Lan, C. E.: The unsteady quasi-vortex-lattice method with application to animal propulsion. Journal of Fluid Mechanics **93**, 747–765 (1979)

11 Usherwood, J. R., Lehmann, F. O.: Phasing of dragonfly wings can improve aerodynamic efficiency by removing swirl. J. R. Soc Interface **5**, 1303–1307 (2008)

12 Maybury, W., Lehmann, F. O.: The fluid dynamics of flight control by kinematic phase lag variation between two robotic insect wings. The Journal of Experimental Biology **207**, 4707–4726 (2004)

13 Yamamoto, M., Isogai, K.: Measurement of unsteady fluid dynamic forces for a mechanical dragonfly model. AIAA Journal **43**, 2475–2480 (2005)

14 Wang, Z., Russell, D.: Effect of forewing and hindwing interactions on aerodynamic forces and power in hovering dragonfly flight. Physical Review Letters **99**, 1–4 (2007)

15 Lan, S. L., Sun, M.: Aerodynamic force and flow structures of two airfoils in flapping motions. Acta Mechanica Sinica **17**, 310–331 (2001)

16 Sun, M., Lan, S. L.: A computational study of the aerodynamic forces and power requirements of dragonfly (Aeschna juncea) hovering. The Journal of Experimental Biology **207**, 1887–1901 (2004)

17 Isogai, K., Fijishiro, S., Saitoh, T., et al.: Unsteady three-dimensional viscous flow simulation of a dragonfly hovering. AIAA Journal **42**, 2053–2059 (2004)

18 Warkentin, J., DeLaurier, J.: Experimental aerodynamic study of tandem flapping membrane wings. Journal of Aircraft **44**, 1653–1651 (2007)

19 Saharon, D., Luttges, M.: Three-dimensional flow produced by a pitching-plunging model dragonfly wing. In: Proc. of the 25th AIAA Aerospace Sciences Meeting, AIAA Paper 87-0121 (1987)

20 Saharon, D., Luttges, M.: Visualization of unsteady separated flow produced by mechanically driven dragonfly wing kinematics model. In: Proceeding of the 26th Aerospace Sciences Meeting, AIAA Paper 88-0569 (1988)

21 Saharon, D., Luttges, M.: Dragonfly unsteady aerodynamic: The role of the wing phase relations in controlling the produced flows. In: Proc. of the 27th AIAA Aerospace Sciences Meeting, AIAA Paper 89-0832 (1989)

22 Akhtar, I., Mittal, R., Lauder G., et al.: Hydrodynamics of a biologically inspired tandem flapping foil configuration. Theoretical and Computational Fluid Dynamics **21**, 155–170 (2007)

23 Huang, H., Sun, M.: Dragonfly forewing-hindwing interaction at various flight speeds and wing phasings. AIAA Journal **45**, 508–511 (2007)

24 Wang, J., Sun, M.: A computational model of the aerodynamics and forewing-hindwing interaction of a model dragonfly in forward flight. The Journal of Experimental Biology **208**, 3785–3804 (2005)

25 Broering, T., Lian, Y., Henshaw, W.: Numerical investigation of energy extraction in a tandem flapping wing configuration. AIAA J. **50**, 2295–2307 (2012)

26 Rival, D., Hass, G., Tropea, C.: Recovery of energy from leading- and trailing-edge vortices in tandem-airfoil configurations. Journal of Aircraft **48**, 203–211 (2011)

27 Lim, K. B., Tay, W. B.: Numerical analysis of the s1020 airfoils in tandem under different flapping configurations. Acta Mech. Sin. **26**, 191–207 (2010)

28 Taylor, G. K., Nudds, R. L., Thomas, A. L. R., et al.: Flying and swimming animals cruise at a strouhal number tuned for high power efficiency. Nature **425**, 707–711 (2003)

29 Henshaw, W. D., Petersson, N. A.: A split-step scheme for the incompressible Navier-Stokes equations. In: Numerical Simulation of Incompressible Flows, World Scientific, River Edge, USA 108–125 (2003)

30 Balay, S., Gropp, W. D., Mcinnes, L. C., et al.: The portable extensible toolkit for scientific computation, Tech.

Rep. http://www.mcs.anl.gov/petsc/petsc.html, Argonne National Laboratory (1999)
31 Young, J.: Numerical simulation of the unsteady aerodynamic flapping airfoils. [Ph.D. Thesis], The University of New South Wales/Australian Defence Force Academy (2005)
32 Young, J., Lai, J., Germain, C.: Simulation and parameter variation of flapping-wing motion based on dragonfly hovering. AIAA Journal **46**, 918–924 (2008)
33 Lian, Y., Shyy, W.: Aerodynamics of low reynolds number plunging airfoil under gusty environment, In: Proc. of the 45th AIAA Aerospace Sciences Meeting and Exhibit, AIAA Paper 2007-71 (2007)
34 Ol, M.: Unsteady aerodynamics for micro air vehicles. NATO RTO AVT-149 Report (2010)
35 Henshaw, W. D., Schwendeman, D. W.: Moving overlapping grids with adaptive mesh refinement for high-speed reactive and non-reactive flow. Journal of Computational Physics **216**, 744–779 (2006)
36 Wakeling, J. M., Ellington, C. P.: Dragonfly flight: II: Velocity, acceleration, and kinematics of flapping flight. The Journal of Experimental Biology **200**, 557–582 (1997)
37 Jones, K. D., Lund, T., Platzer, M. F., et al.: Experimental and computational investigation of flapping wing propulsion for micro air vehicles. Progress in Astronautics and Aeronautics **195**, 307–339 (2001)
38 Ramamurti, R., Sandberg, W.: Simulation of flow about flapping airfoils using finite element incompressible flow solver. AIAA Journal **39**, 253–260 (2001)